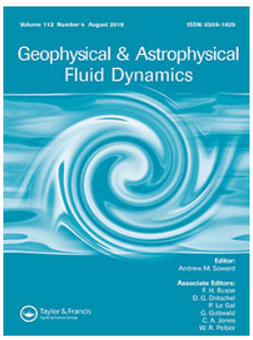

Taylor & Francis
Taylor & Francis Group

Geophysical & Astrophysical Fluid Dynamics

ISSN: 0309-1929 (Print) 1029-0419 (Online) Journal homepage: https://www.tandfonline.com/loi/ggaf20

Evolution of aligned states within nonlinear dynamos

D. Miller

To cite this article: D. Miller (2019) Evolution of aligned states within nonlinear dynamos, Geophysical & Astrophysical Fluid Dynamics, 113:4, 405-423, DOI: 10.1080/03091929.2019.1640876

To link to this article: https://doi.org/10.1080/03091929.2019.1640876

Published online: 29 Jul 2019.

GEOPHYSICAL & ASTROPHYSICAL FLUID DYNAMICS
2019, VOL. 113, NO. 4, 405–423
https://doi.org/10.1080/03091929.2019.1640876

Taylor & Francis
Taylor & Francis Group

Evolution of aligned states within nonlinear dynamos

D. Miller

College of Engineering, Mathematics and Physical Sciences, University of Exeter, Exeter, UK

ABSTRACT
The Archontis dynamo is a rare example of an MHD dynamo within which forcing drives a dynamo where the flow and magnetic fields are almost perfectly aligned and the energies are approximately equal. In this paper, I expand upon our knowledge of the dynamo by showing that the intermediate steady states of the kinetic and magnetic energies observed by Cameron and Galloway are not a necessary feature of aligned dynamos. Furthermore, I show that the steady state into which the flow and magnetic fields eventually evolve is remarkably robust to the addition of time dependence and asymmetry to the forcing.

ARTICLE HISTORY
Received 14 January 2019
Accepted 3 July 2019

KEYWORDS
Dynamo theory; MHD

1. Introduction

The work of Larmor (1919) is widely believed to be the first to propose the idea that observed astrophysical magnetic fields could be obtained by an amplification of a seed magnetic field through a dynamo process whereby growth of the magnetic field is induced by the motion of a flow. In the case of an incompressible flow, this may be stated mathematically as follows:

$$\frac{\partial \boldsymbol{u}}{\partial t} + \boldsymbol{u}\cdot\nabla\,\boldsymbol{u} = -\nabla p + \boldsymbol{j}\times\boldsymbol{B} + \nu\nabla^2\boldsymbol{u} + \boldsymbol{F}, \tag{1a}$$

$$\frac{\partial \boldsymbol{B}}{\partial t} = \nabla\times(\boldsymbol{u}\times\boldsymbol{B}) + \eta\nabla^2\boldsymbol{B}, \tag{1b}$$

$$0 = \nabla\cdot\boldsymbol{B}, \tag{1c}$$

$$0 = \nabla\cdot\boldsymbol{u}. \tag{1d}$$

Here (1a) and (1b) govern the evolution of the flow and magnetic field respectively, while (1c) is solenoidal condition on the magnetic field and (1d) is the incompressible condition on the flow. In them, $\boldsymbol{u}$ is the flow, p the pressure, $\boldsymbol{B}$ is the magnetic field, $\boldsymbol{j} = \nabla\times\boldsymbol{B}$ and $\boldsymbol{F}$ is a forcing. The diffusion constants, ν and η, take fixed values and can be thought of as inverse Reynolds (ν) and magnetic Reynolds (η) numbers. The evolution of these equations (when initialised with a prescribed forcing, a prescribed flow and a seed magnetic field) can be broadly split into three regimes (see, e.g. Tanner and Hughes 2003). In the

CONTACT D. Miller dm473@exeter.ac.uk

first stage, the magnetic field is weak and thus the Lorentz force term within (1a) can be neglected. Due to the linearity of (1b), the magnetic field must then either exponentially grow or decay with the exponentially growing solutions being those that are required to eventually achieve a significant magnetic energy budget.

Eventually, the exponentially growing magnetic field is sufficiently strong that the Lorentz force term is no longer weak and begins to have an impact upon the flow. In this second (nonlinear) regime, either or both of the magnetic and flow fields undergo changes that halt the exponential growth of the magnetic field and, in a successful dynamo, cause the magnetic field to saturate. The saturation of the dynamo has predominantly been found (Tanner and Hughes 2003) to be achieved either via a reduction in the chaotic properties of the flow, thus reducing magnetic field enhancement via stretching, or a reduction in the length scales of the magnetic field, thus enhancing diffusion. One potential problem, however, is that the magnetic field structure that is found once saturation is achieved, is predominantly filamentary in nature. This problem is discussed within (Galloway 2003, 2012) with scaling arguments leading to the conclusion that in the limit of small η and ν the magnetic energy must become negligible compared to the kinetic energy.

A small number of examples of non-filamentary dynamos have been found, with the most widely studied being the Archontis dynamo. In his PhD thesis (Archontis 2000) and a subsequent paper (Dorch and Archontis 2004) Archontis found that the forcing

$$\boldsymbol{F}_A = \nu \left[\sin z,\ \sin x,\ \sin y\right] \tag{2}$$

produces a dynamo where the magnetic and kinetic energies are almost exactly at equipartition for unit $P_m = \nu/\eta$ and where each of the fields is almost exactly $\boldsymbol{F}_A/2\nu$. Further investigation was performed within Cameron and Galloway (2006a, 2006b) with a simpler system and an incompressible flow. The authors found that the magnetic and flow fields at saturation of the Archontis dynamo are non-filamentary in nature and therefore the magnetic energy may remain significant as η and ν become small.

Furthermore, Cameron and Galloway (2006a) (see figure 19 of their paper or figure 1 of this paper) found that amplification of a seed magnetic field by the Archontis dynamo yields an interesting result whereby the magnetic and flow fields appear to saturate at a statistically steady state (SSS) but then at a later time experience a second growth phase and arrive at a second state where the flow and magnetic fields are in almost perfect alignment. In figure 1, I show results of a numerical simulation with the same qualitative features as figure 19 of Cameron and Galloway (2006a). The kinetic energy *KE* and magnetic energy *ME*, respectively

$$KE = \frac{1}{8\pi^3}\int_V \frac{\boldsymbol{u}^2}{2}\,\mathrm{d}V, \quad ME = \frac{1}{8\pi^3}\int_V \frac{\boldsymbol{B}^2}{2}\,\mathrm{d}V, \tag{3a,b}$$

values are on the left axis, whereas the alignment measure

$$H_1 = \frac{1}{8\pi^3}\frac{1}{\sqrt{ME}\sqrt{KE}}\left|\int_V \frac{\boldsymbol{u}\cdot\boldsymbol{B}}{2}\mathrm{d}V\right| \tag{4}$$

values are on the right axis.

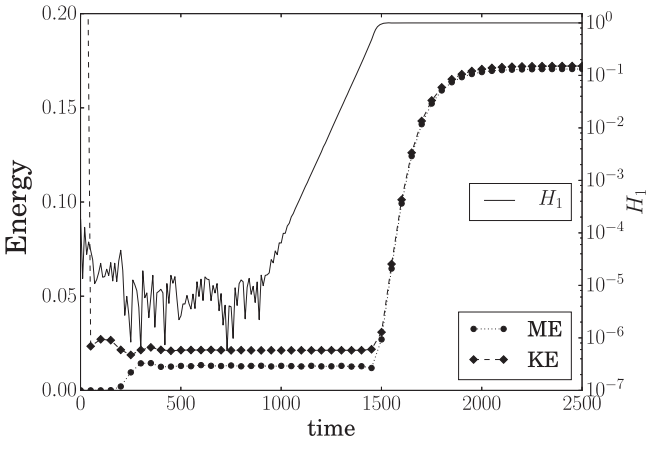

Figure 1. Plot from a numerical simulation showing kinetic and magnetic energy as well as alignment measure H_1, shown in (4). The three quantities shown have the same behaviour as those shown within figure 19 of Cameron and Galloway (2006a). Two saturation states are seen for the energies, one for $t \in (200, 1500)$ and one for $t > 1700$. The continued evolution of the alignment during the first statistically steady state is a clear indicator that the fields have yet to finish evolving.

We see that even though the kinetic and magnetic energies appear to have saturated to a SSS the magnetic and flow fields become increasingly aligned until they become almost perfectly aligned. At this point, a second growth phase occurs with final saturation being at a truly steady state where $\boldsymbol{u}$ and $\boldsymbol{B}$ are almost exactly $\boldsymbol{F}_A/2\nu$. The question can then be asked whether or not the SSS is crucial to achieving the final steady state and, if not, why it exists at all.

Further investigation of the Archontis dynamo within Cameron and Galloway (2006a) predominantly concerned the saturated kinetic and magnetic energies and therefore used initial condition $\boldsymbol{u} = \boldsymbol{B} = \boldsymbol{F}_A/\nu$. It was found that the kinetic and magnetic energies for unit P_m appear to saturate as η and ν become small with $\eta = \nu = 1/800$ being the smallest investigated. Furthermore, it was found that a forcing can be specified which yields an arbitrary ratio of kinetic and magnetic energies. Further investigation of the Archontis dynamo was performed within Archontis *et al.* (2007), Galloway (2010), Gilbert *et al.* (2011), and in a review article on ABC flows, Galloway (2012). Key results include: the key role played by diffusive terms nearby stagnation points of the flow (Gilbert *et al.* 2011), and the identification (Galloway 2012) that the Archontis dynamo must saturate on a diffusive timescale. However, the reason for the existence of the SSS in figure 1 remains an open question, as does the ubiquity of nonlinear dynamos which are aligned ($H_1 \approx 1$) and at equipartition ($ME \approx KE$).

I outline equations and numerical details within section 2. In section 3, I seek to understand why the SSS exists in figure 1, with the aim of determining whether or not its presence is significant to the evolution of the dynamo. In section 4, I examine how the alignment within the dynamo evolves by examining the alignment evolution equation. In section 5, I examine how the pointwise distribution of alignment changes. Finally, in section 6, I introduce time dependence and asymmetry to the Archontis forcing to test the robustness of achieving an equipartition aligned dynamo.

2. Equations and numerics

The equations to be solved are the equations governing the motion of the flow field (1a) and the induction equation (1b), which governs the evolution of the magnetic field. The magnetic field is solenoidal (1c) and the flow is incompressible (1d).

Alignment of the magnetic field and the flow is measured by quantity (4), which gives the cross-helicity normalised by the energies as used within Cameron and Galloway (2006a). The numerical methods used within sections 3, 5 and 6 are the same. Equations (1a,b) are solved using a pseudo-spectral code. Incompressibility is maintained at each timestep via a projection method. The resolution used is $64 \times 64 \times 64$. The diffusion terms within equations (1a,b) are integrated exactly and an Adams-Bashforth: Adams–Moulton predictor–corrector method is used to timestep the other terms within both equations. A number of tests were performed to check the code against the work within Galanti *et al.* (1992) and Cameron and Galloway (2006a) with good agreement found.

3. Existence of a statistically steady state

In this section, I examine the origins of the SSS seen in figure 1. As my initial results did not show the SSS, initial conditions must be playing a role. The initial condition for the flow, $\boldsymbol{u}_0 = \boldsymbol{F}_A/\nu$, and the diffusivities, $\eta^{-1} = \nu^{-1} = 100$, are set. Therefore, it is only variation in the composition of the initial magnetic field that can change whether or not the SSS appears. It is this which I will examine.

The magnetic field is specified in terms of its Fourier modes, $\hat{\boldsymbol{B}}_{\boldsymbol{k}} = \hat{\boldsymbol{B}}^R_{\boldsymbol{k}} + \mathrm{i}\hat{\boldsymbol{B}}^I_{\boldsymbol{k}}$, where $\hat{\boldsymbol{B}}^R_{\boldsymbol{k}}$ and $\hat{\boldsymbol{B}}^I_{\boldsymbol{k}}$ are real functions. The real and imaginary components of $\hat{\boldsymbol{B}}_{\boldsymbol{k}}$ are separately assigned a value at each Fourier mode $\boldsymbol{k} = [k_x, k_y, k_z]$ according to a random normal distribution. $\hat{\boldsymbol{B}}^R_{\boldsymbol{k}}$ and $\hat{\boldsymbol{B}}^I_{\boldsymbol{k}}$ are then multiplied by a power of 10 so that the relative order of magnitudes of the real and imaginary parts can be altered, resulting in the respective order of magnitudes

$$\mathrm{O}\left(\hat{\boldsymbol{B}}^R_{\boldsymbol{k}}\right) = 10^a, \qquad \mathrm{O}\left(\hat{\boldsymbol{B}}^I_{\boldsymbol{k}}\right) = 10^b. \tag{5a,b}$$

The parameters a and b are chosen to vary between -4 and -8 so that the initial magnetic field is weak. The cases where $\hat{\boldsymbol{B}}$ had no real or imaginary component, $a, b = -\infty$, were also examined. For reasons that become apparent later, I define the energy within the even (E_{BR}) and odd (E_{BI}) components of the magnetic field by

$$E_{BR} = \sum_{\boldsymbol{k}} \left|\hat{\boldsymbol{B}}^R_{\boldsymbol{k}}\right|^2, \qquad E_{BI} = \sum_{\boldsymbol{k}} \left|\hat{\boldsymbol{B}}^I_{\boldsymbol{k}}\right|^2 \tag{6a,b}$$

and the equivalent energies for the flow by

$$E_{UR} = \sum_{\boldsymbol{k}} \left|\hat{\boldsymbol{u}}^R_{\boldsymbol{k}}\right|^2, \qquad E_{UI} = \sum_{\boldsymbol{k}} \left|\hat{\boldsymbol{u}}^I_{\boldsymbol{k}}\right|^2, \tag{6c,d}$$

where $\hat{\boldsymbol{u}}_{\boldsymbol{k}} = \hat{\boldsymbol{u}}^R_{\boldsymbol{k}} + \mathrm{i}\hat{\boldsymbol{u}}^I_{\boldsymbol{k}}$.

As noted by Gilbert *et al.* (2011), the initial flow, the forcing and the final flow and magnetic field are invariant under the inversion symmetry $j(-x, -y, -z)$ and thus have

the property $\boldsymbol{A}(\boldsymbol{x}) = -\boldsymbol{A}(-\boldsymbol{x})$, where $\boldsymbol{A}$ is a vector field. Furthermore, if $a = -\infty$, then the initial magnetic field obeys the same symmetry, whereas if $b = -\infty$ then the initial seed magnetic field has the symmetry $\boldsymbol{A}(\boldsymbol{x}) = \boldsymbol{A}(-\boldsymbol{x})$. As such, variation in the value of a and b also has the effect of altering the symmetry properties of the initial magnetic field. I also note that if $\boldsymbol{B}$ is a solution of the MHD equations, then so is $-\boldsymbol{B}$ due to a symmetry of the equations.

In varying a and b, I find that the SSS is only observed where the initial magnetic field has no imaginary component ($b = -\infty$). I define these runs as Group A and an example is shown within figure 2(a,b). In figure 2(a), I show the energies and the alignment and in figure 2(b) I show the amount of the magnetic field in the even and odd parts of the magnetic field. We see in figure 2(a) that the flow and magnetic fields become aligned a short time before the second growth phase occurs. In figure 2(b), we see that before the alignment begins to grow the energy in the odd component of the magnetic field is growing and becomes larger than the energy in the even component as the alignment becomes maximal.

For initial conditions where the real component is much larger than the imaginary component, a short state that is close to being statistically steady is obtained (see $t \in (200, 300)$ in figure 2 c). I define these runs as Group B and an example is shown within figure 2(c,d). As with the Group A runs, we see a second growth phase in the energy once the two fields have become aligned in figure 2(c). In figure 2(d), we also see similar behaviour to the Group A run with the energy in the odd component of the magnetic field becoming larger than that in the even component immediately prior to the second growth phase.

All other initial conditions examined (those for which the initial $\hat{\boldsymbol{B}}_{\boldsymbol{k}}^{I}$ is not zero or extremely weak) yield magnetic and flow fields which saturate to the second steady state without an earlier SSS. I define these runs as Group C and an example is shown within figure 2(e,f). Figure 2(e) shows the alignment and energies. We see that the alignment immediately approaches its maximal value and that the magnetic and kinetic energies take less time than the Group A and Group B runs to saturate. In figure 2(f), we see that the energy in the odd component is quickly larger than that within the even component.

Comparing Group A runs to the Group B and Group C runs gives insights into the necessary criterion for when we expect to see a SSS. The final saturated state has been shown by Cameron and Galloway to be close to $\frac{1}{2}[\sin z, \sin x, \sin y]$, thus the energy is almost wholly within the odd component of the field, i.e. where E_{BR} is much weaker than E_{BI}. The magnetic field initiated with initial conditions in Group A and Group B thus has to evolve from having energy predominantly within the even component to having energy wholly within its odd component.

I will now use the Fourier space form of the MHD equations to show why the Group A runs have a SSS. The equations are

$$\frac{\partial \hat{\boldsymbol{B}}_{\boldsymbol{k}}}{\partial t} + \eta \boldsymbol{k}^2 \hat{\boldsymbol{B}}_{\boldsymbol{k}} = \mathrm{i}\boldsymbol{k} \times \sum_{\boldsymbol{m}} \left(\hat{\boldsymbol{u}}_{\boldsymbol{k}-\boldsymbol{m}} \times \hat{\boldsymbol{B}}_{\boldsymbol{m}} \right), \tag{7a}$$

$$\frac{\partial \hat{\boldsymbol{u}}_{\boldsymbol{k}}}{\partial t} + \nu \boldsymbol{k}^2 \hat{\boldsymbol{u}}_{\boldsymbol{k}} = \mathrm{i}\hat{\boldsymbol{F}}_{\boldsymbol{k}}^{R} + \mathrm{i}\boldsymbol{P} \sum_{\boldsymbol{m}} \left(\hat{\boldsymbol{u}}_{\boldsymbol{k}-\boldsymbol{m}} \times \left(\boldsymbol{m} \times \hat{\boldsymbol{u}}_{\boldsymbol{m}} \right) - \hat{\boldsymbol{B}}_{\boldsymbol{k}-\boldsymbol{m}} \times \left(\boldsymbol{m} \times \hat{\boldsymbol{B}}_{\boldsymbol{m}} \right) \right). \tag{7b}$$

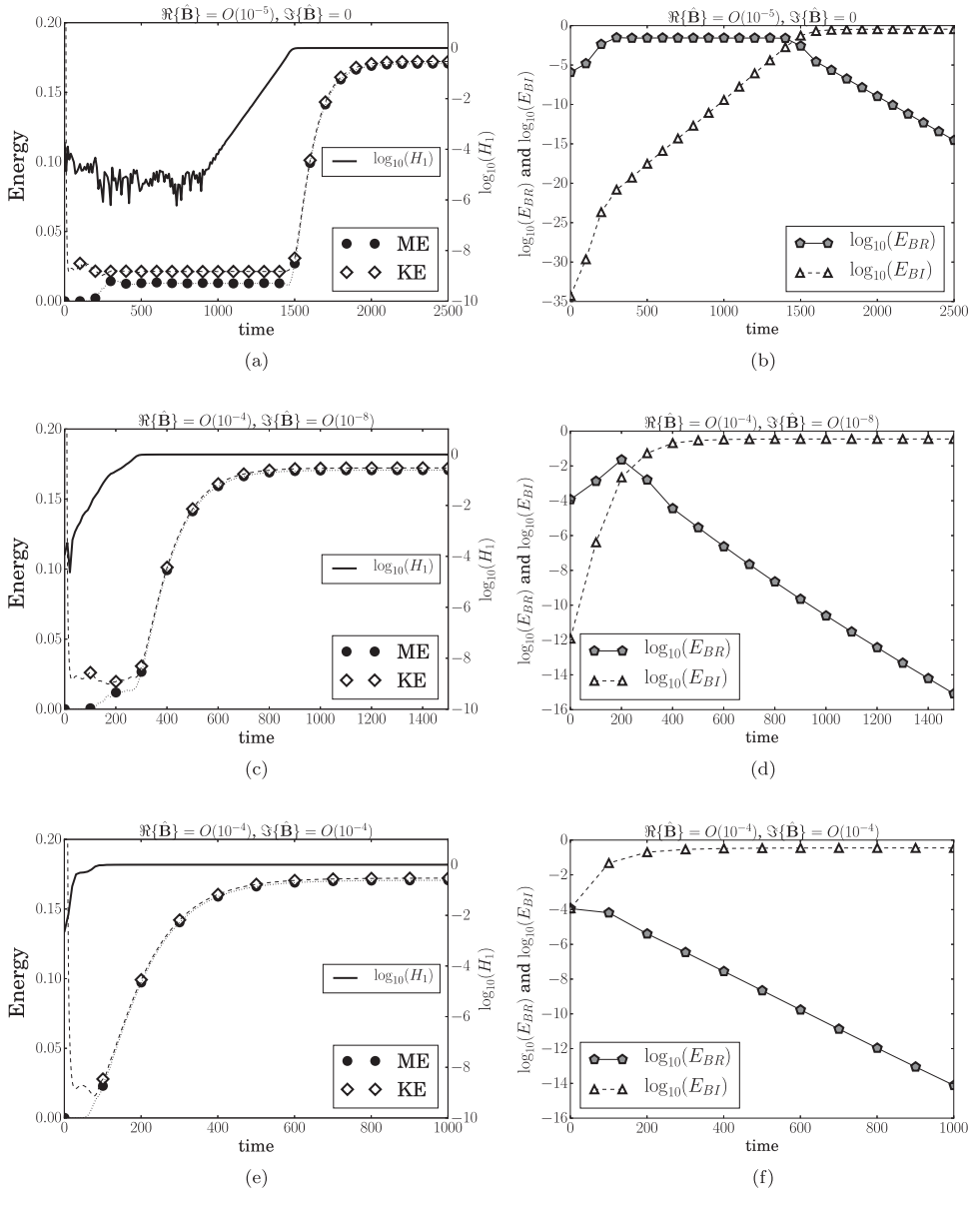

Figure 2. Plots of energy, alignment and quantities (6aa,b) for a variety of initial conditions: (a) Group A, (b) Group A, (c) Group B, (d) Group B, (e) Group C, (f) Group C.

Incompressibility is used to define the projection operator $\boldsymbol{P}$ which in index notation is given by $P_{ij} = \delta_{ij} - k_i k_j/(k_l k_l)$. The forcing is written in terms of a real function $\hat{\boldsymbol{F}}^R_{\boldsymbol{k}}$. The general forms of $\hat{\boldsymbol{u}}_{\boldsymbol{k}}$ and $\hat{\boldsymbol{B}}_{\boldsymbol{k}}$ are given by $\hat{\boldsymbol{u}}_{\boldsymbol{k}} = \hat{\boldsymbol{u}}^R_{\boldsymbol{k}} + \mathrm{i}\hat{\boldsymbol{u}}^I_{\boldsymbol{k}}$ and $\hat{\boldsymbol{B}}_{\boldsymbol{k}} = \hat{\boldsymbol{B}}^R_{\boldsymbol{k}} + \mathrm{i}\hat{\boldsymbol{B}}^I_{\boldsymbol{k}}$ respectively with all functions being real. Substitution of $\hat{\boldsymbol{u}}_{\boldsymbol{k}}$ and $\hat{\boldsymbol{B}}_{\boldsymbol{k}}$ into (7) yields evolution equations for $\hat{\boldsymbol{u}}^R_{\boldsymbol{k}}$, $\hat{\boldsymbol{u}}^I_{\boldsymbol{k}}$, $\hat{\boldsymbol{B}}^R_{\boldsymbol{k}}$ and $\hat{\boldsymbol{B}}^I_{\boldsymbol{k}}$. Substitution of the initial conditions of the Group A run into these

equations then yields

$$\frac{\partial \hat{\boldsymbol{B}}_{\boldsymbol{k}}^{R}}{\partial t} + \eta \boldsymbol{k}^2 \hat{\boldsymbol{B}}_{\boldsymbol{k}}^{R} = -\boldsymbol{k} \times \sum_{\boldsymbol{m}} \left(\hat{\boldsymbol{u}}_{\boldsymbol{k}-\boldsymbol{m}}^{I} \times \hat{\boldsymbol{B}}_{\boldsymbol{m}}^{R} \right), \tag{8a}$$

$$\frac{\partial \hat{\boldsymbol{u}}_{\boldsymbol{k}}^{I}}{\partial t} + \nu \boldsymbol{k}^2 \hat{\boldsymbol{u}}_{\boldsymbol{k}}^{I} = \hat{\boldsymbol{F}}_{\boldsymbol{k}}^{R} - \boldsymbol{P} \sum_{\boldsymbol{m}} \left(\hat{\boldsymbol{u}}_{\boldsymbol{k}-\boldsymbol{m}}^{I} \times \left(\boldsymbol{m} \times \hat{\boldsymbol{u}}_{\boldsymbol{m}}^{I} \right) + \hat{\boldsymbol{B}}_{\boldsymbol{k}-\boldsymbol{m}}^{R} \times \left(\boldsymbol{m} \times \hat{\boldsymbol{B}}_{\boldsymbol{m}}^{R} \right) \right), \tag{8b}$$

$$\frac{\partial \hat{\boldsymbol{B}}_{\boldsymbol{k}}^{I}}{\partial t} = 0, \tag{8c}$$

$$\frac{\partial \hat{\boldsymbol{u}}_{\boldsymbol{k}}^{R}}{\partial t} = 0. \tag{8d}$$

Equations (8c,d) then show that if $\hat{\boldsymbol{B}}_{\boldsymbol{k}}$ is initially real and $\hat{\boldsymbol{u}}_{\boldsymbol{k}}$ is initially imaginary (as is the case for Group A runs) then they will remain so.

The Group A evolution that we see can therefore be explained as follows. Initially, the magnetic field is even and the flow is odd and so the system does not evolve to the solution observed for the other initial conditions as the odd component of the magnetic field cannot grow. The fields thus evolve to the SSS and remain there for a large number of timesteps. During this period, the dot product of the flow and magnetic fields is odd and so H_1 is necessarily zero. However, as the numerical simulation evolves, numerical rounding errors cause the imaginary component of $\hat{\boldsymbol{B}}$ to become non-zero and it then grows in time. When this happens, a symmetry breaking occurs and the magnetic field transitions to a second state where it is now odd. This transition is captured by H_1 due to the quantity increasing from zero as the imaginary component of $\hat{\boldsymbol{B}}$ grows, hence the quantity's remarkable ability to pre-empt the second growth phase.

This behaviour may also be explained using symmetry properties. Equations (8) show that the symmetries in the initial condition, $\boldsymbol{u}_0(\boldsymbol{x}) = -\boldsymbol{u}_0(-\boldsymbol{x})$ and $\boldsymbol{B}_0(\boldsymbol{x}) = \boldsymbol{B}_0(-\boldsymbol{x})$, are preserved. Preservation of symmetries has previously been examined by Krstulovic *et al.* (2011) who showed that the MHD equations are invariant under the reflection symmetry operator, provided that the flow and the forcing are odd and the magnetic field is either odd or even. Equations (8) are therefore the Fourier equivalents to equations (17) and (18) in section II.B of Krstulovic *et al.* (2011). Showing that the imaginary component of $\hat{\boldsymbol{B}}$ and the real component of $\hat{\boldsymbol{u}}$ do not grow provided they are zero initially within equations (8) is therefore equivalent to stating that the odd symmetry of the magnetic field is preserved by the MHD equations. This symmetry is only broken when numerics introduce small amounts of $\hat{\boldsymbol{B}}^{I}$ and $\hat{\boldsymbol{u}}^{R}$, which then rapidly grow as the system is attracted to a state where the magnetic field is dominated by its $\hat{\boldsymbol{B}}^{I}$ component.

In summary, the SSS observed within Cameron and Galloway (2006a) is present only due to particular symmetry properties of a subset of initial conditions. As a result is not expected to be a general property of dynamos with high amounts of alignment.

4. Evolution of alignment

In this section, I examine the evolution of the alignment and its relationship with the weak components of the flow and magnetic field. I also address the origins of the time-dependent

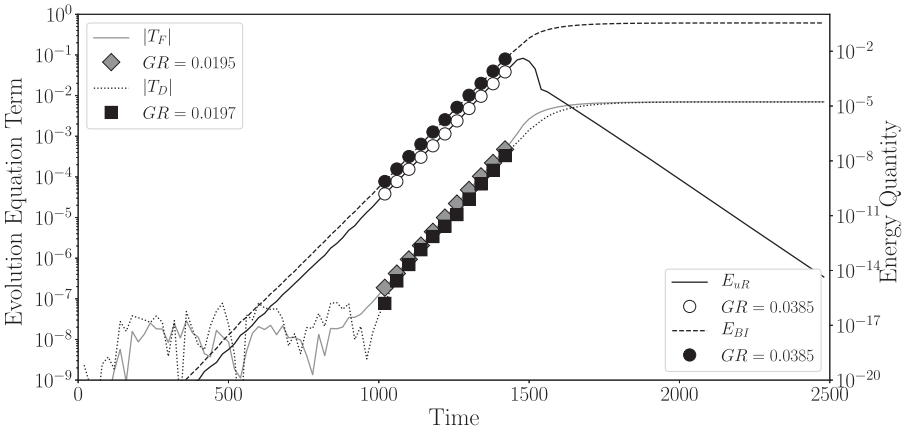

Figure 3. Plot showing the absolute value of the terms on the right side of (9b) (left axis) and the energy in the even part of the flow (6ac) and the odd part of the magnetic field (6ab) (right axis). The growth rates (GR) in the legends indicate the GR of the quantity directly above. For example, the diamonds indicate the GR for $|T_F|$. Initially during the first SSS the cross-helicity evolution terms are statistically steady with an approximate balance between the forcing and diffusion terms resulting in no growth in alignment up until $t = 1000$. Throughout the first SSS, however, E_{UR} and E_{BI} are growing exponentially due to exponential growth in $\hat{\boldsymbol{B}}^I_{\boldsymbol{k}}$ and $\hat{\boldsymbol{u}}^R_{\boldsymbol{k}}$. At $t \approx 1000$, the exponential growth rate of $\hat{\boldsymbol{B}}^I_{\boldsymbol{k}}$ and $\hat{\boldsymbol{u}}^R_{\boldsymbol{k}}$ is then felt by the cross-helicity evolution terms which begin to grow in magnitude (T_D is negative) with the same growth rate as $\hat{\boldsymbol{B}}^I_{\boldsymbol{k}}$ and $\hat{\boldsymbol{u}}^R_{\boldsymbol{k}}$.

behaviour of $\hat{\boldsymbol{B}}^I_{\boldsymbol{k}}$ and $\hat{\boldsymbol{u}}^R_{\boldsymbol{k}}$. As outlined in Galloway (2012), a cross-helicity evolution equation may be found by taking the dot product of (1a) with $\boldsymbol{B}$, taking the dot product of (1b) with $\boldsymbol{u}$, summing the two and integrating over the volume. The remaining non-zero terms are shown in

$$\frac{\mathrm{d}}{\mathrm{d}t}\int_V u_i B_i \,\mathrm{d}V = \int_V F_i B_i \mathrm{d}V - (\eta + \nu)\int_V \frac{\partial u_i}{\partial x_j}\frac{\partial B_i}{\partial x_j}\,\mathrm{d}V \tag{9a}$$

(index summation notation used), while

$$T = T_F + T_D \tag{9b}$$

shows the nomenclature that I will use for each of the terms.

It is interesting to understand which of the terms on the right-hand side of (9b) are responsible for the rapid growth of alignment seen in the second half of the SSS in a Group A run. In figure 3, I plot the absolute value of the terms on the right side of (9b) (left axis) and the energy in the even part of the flow (6ac) and the odd part of the magnetic field (6ab) (right axis). Examination of each of these quantities identified a period of time where the quantities grow exponentially and so the growth rates have also been added. Growth rates are calculated using a linear least squares fit. The growth rates (GR) in the legends indicate the GR of the quantity directly above. For example, the diamonds indicate the GR for $|T_F|$.

I first consider the cross-helicity evolution (left axis) in figure 3 only. We see that from arriving at the SSS until $t \approx 1000$ the forcing and diffusive terms are weak with no overall change to the alignment. However, at $t \approx 1000$ the magnitude of the terms begins to grow exponentially with almost identical growth rates. From $t \approx 1000$ to $t \approx 1500$, T_F is larger

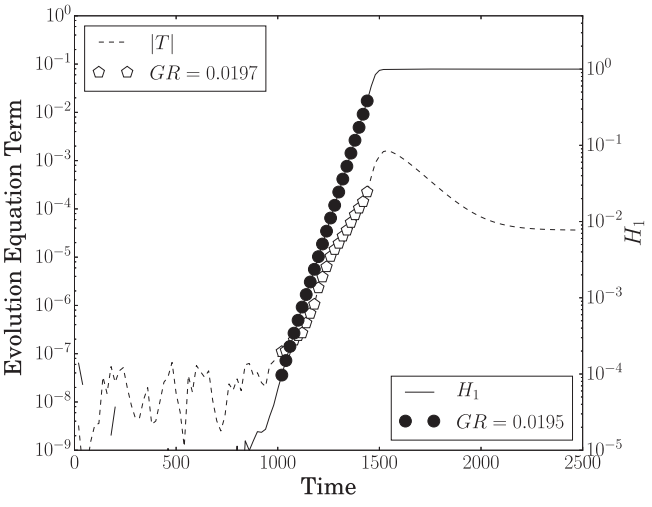

Figure 4. Plot of $|T|$ (left axis) and H_1 (right axis). Both grow exponentially prior to the jump to the second SSS for the energies.

(and positive) than T_D, although both quantities are growing exponentially with an almost identical growth rate. This results in exponential growth of T and subsequently exponential growth of H_1, as shown in figure 4. This continues until $t \approx 1500$ where growth in $|T_D|$, relative to T_F, results in a balance of the forcing and diffusion terms within the cross-helicity equation and a subsequent saturation of the alignment value. As such, growth in alignment can be thought of as being a result of domination of T_F over T_D within (9b). However, this alone does not explain the exponential growth of H_1 and the terms within (9b).

To explain this, consider the right axis of figure 3. E_{UR} and E_{BI} grow exponentially with a fixed growth rate as soon as the energies enter the SSS. Until $t \approx 1000$, however, this exponential growth has little effect on the alignment as E_{UR} and E_{BI} are weak. After this, we see all of the alignment evolution quantities, as well as the alignment, begin to grow exponentially with the same growth rate as $\hat{\boldsymbol{B}}^I_{\boldsymbol{k}}$ and $\hat{\boldsymbol{u}}^R_{\boldsymbol{k}}$ (half that of E_{UR} and E_{BI}). This continues until $t \approx 1500$ where alignment becomes close to maximal, and the energies begin to grow rapidly. Exponential growth of the quantities in (9b) and H_1 therefore appears to originate with $\hat{\boldsymbol{B}}^I_{\boldsymbol{k}}$ and $\hat{\boldsymbol{u}}^R_{\boldsymbol{k}}$.

To understand the exponential growth of $\hat{\boldsymbol{B}}^I_{\boldsymbol{k}}$ and $\hat{\boldsymbol{u}}^R_{\boldsymbol{k}}$ consider the full evolution equations

$$\frac{\partial \hat{\boldsymbol{B}}^R_{\boldsymbol{k}}}{\partial t} + \eta \boldsymbol{k}^2 \hat{\boldsymbol{B}}^R_{\boldsymbol{k}} = -\boldsymbol{k} \times \sum_{\boldsymbol{m}} \left[\left(\hat{\boldsymbol{u}}^I_{\boldsymbol{k}-\boldsymbol{m}} \times \hat{\boldsymbol{B}}^R_{\boldsymbol{m}} \right) + \left(\hat{\boldsymbol{u}}^R_{\boldsymbol{k}-\boldsymbol{m}} \times \hat{\boldsymbol{B}}^I_{\boldsymbol{m}} \right) \right], \tag{10a}$$

$$\frac{\partial \hat{\boldsymbol{B}}^I_{\boldsymbol{k}}}{\partial t} + \eta \boldsymbol{k}^2 \hat{\boldsymbol{B}}^I_{\boldsymbol{k}} = \boldsymbol{k} \times \sum_{\boldsymbol{m}} \left[\left(\hat{\boldsymbol{u}}^R_{\boldsymbol{k}-\boldsymbol{m}} \times \hat{\boldsymbol{B}}^R_{\boldsymbol{m}} \right) - \left(\hat{\boldsymbol{u}}^I_{\boldsymbol{k}-\boldsymbol{m}} \times \hat{\boldsymbol{B}}^I_{\boldsymbol{m}} \right) \right], \tag{10b}$$

$$\begin{aligned} \frac{\partial \hat{\boldsymbol{u}}^R_{\boldsymbol{k}}}{\partial t} + \nu \boldsymbol{k}^2 \hat{\boldsymbol{u}}^R_{\boldsymbol{k}} = \boldsymbol{P} \sum_{\boldsymbol{m}} \Big[& -\hat{\boldsymbol{u}}^R_{\boldsymbol{k}-\boldsymbol{m}} \times \left(\boldsymbol{m} \times \hat{\boldsymbol{u}}^I_{\boldsymbol{m}} \right) - \hat{\boldsymbol{u}}^I_{\boldsymbol{k}-\boldsymbol{m}} \times \left(\boldsymbol{m} \times \hat{\boldsymbol{u}}^R_{\boldsymbol{m}} \right) \\ & + \hat{\boldsymbol{B}}^R_{\boldsymbol{k}-\boldsymbol{m}} \times \left(\boldsymbol{m} \times \hat{\boldsymbol{B}}^I_{\boldsymbol{m}} \right) + \hat{\boldsymbol{B}}^I_{\boldsymbol{k}-\boldsymbol{m}} \times \left(\boldsymbol{m} \times \hat{\boldsymbol{B}}^R_{\boldsymbol{m}} \right) \Big], \end{aligned} \tag{10c}$$

$$\frac{\partial \hat{\boldsymbol{u}}_{\boldsymbol{k}}^{I}}{\partial t} + \nu \boldsymbol{k}^2 \hat{\boldsymbol{u}}_{\boldsymbol{k}}^{I} = \boldsymbol{P} \sum_{\boldsymbol{m}} \Big[\hat{\boldsymbol{u}}_{\boldsymbol{k}-\boldsymbol{m}}^{R} \times \Big(\boldsymbol{m} \times \hat{\boldsymbol{u}}_{\boldsymbol{m}}^{R} \Big) - \hat{\boldsymbol{u}}_{\boldsymbol{k}-\boldsymbol{m}}^{I} \times \Big(\boldsymbol{m} \times \hat{\boldsymbol{u}}_{\boldsymbol{m}}^{I} \Big) - \hat{\boldsymbol{B}}_{\boldsymbol{k}-\boldsymbol{m}}^{R} \times \Big(\boldsymbol{m} \times \hat{\boldsymbol{B}}_{\boldsymbol{m}}^{R} \Big) + \hat{\boldsymbol{B}}_{\boldsymbol{k}-\boldsymbol{m}}^{I} \times \Big(\boldsymbol{m} \times \hat{\boldsymbol{B}}_{\boldsymbol{m}}^{I} \Big) \Big] + \hat{\boldsymbol{F}}_{\boldsymbol{k}}^{R} \tag{10d}$$

for the real and imaginary components of the two fields. When $\hat{\boldsymbol{B}}_{\boldsymbol{k}}^{I}$ and $\hat{\boldsymbol{u}}_{\boldsymbol{k}}^{R}$ are weak they have little effect on the evolution of $\hat{\boldsymbol{B}}_{\boldsymbol{k}}^{R}$ and $\hat{\boldsymbol{u}}_{\boldsymbol{k}}^{I}$ and so equations (10a,d) initially evolve independently of these quantities.

However, equations (10b,c) are linear in $\hat{\boldsymbol{B}}_{\boldsymbol{k}}^{I}$ and $\hat{\boldsymbol{u}}_{\boldsymbol{k}}^{R}$. As such, these equations admit exponentially growing solutions for $\hat{\boldsymbol{B}}_{\boldsymbol{k}}^{I}$ and $\hat{\boldsymbol{u}}_{\boldsymbol{k}}^{R}$ (with the quantities having the same growth rate) and this is what is observed in figure 3. As a result, the exponential growth phase of $\hat{\boldsymbol{B}}_{\boldsymbol{k}}^{I}$ and $\hat{\boldsymbol{u}}_{\boldsymbol{k}}^{R}$ is not too dissimilar to the kinematic growth phase of the full magnetic field at the beginning of a nonlinear dynamo.

To show how exponential growth in $\hat{\boldsymbol{B}}_{\boldsymbol{k}}^{I}$ and $\hat{\boldsymbol{u}}_{\boldsymbol{k}}^{R}$ then leads to exponential growth in H_1 with the same growth rate, I assume that the small parts of the magnetic and flow field depend exponentially upon time so that $\hat{\boldsymbol{B}}_{\boldsymbol{k}}(t) = \hat{\boldsymbol{B}}_{\boldsymbol{k}}^{R}(t) + \mathrm{i}\hat{\boldsymbol{B}}_{\boldsymbol{k}}^{I} \exp(\sigma t)$ and $\hat{\boldsymbol{u}}_{\boldsymbol{k}}(t) = \hat{\boldsymbol{u}}_{\boldsymbol{k}}^{R} \exp(\sigma t) + \mathrm{i}\hat{\boldsymbol{u}}_{\boldsymbol{k}}^{I}(t)$. The magnetic *ME* and kinetic *KE* energies are then

$$ME = \frac{1}{2} \sum_{\boldsymbol{k}} \hat{\boldsymbol{B}}_{\boldsymbol{k}} \hat{\boldsymbol{B}}_{\boldsymbol{k}}^{\star} = \frac{1}{2} \sum_{\boldsymbol{k}} \Big[\hat{\boldsymbol{B}}_{\boldsymbol{k}}^{R} \hat{\boldsymbol{B}}_{\boldsymbol{k}}^{R} + \hat{\boldsymbol{B}}_{\boldsymbol{k}}^{I} \hat{\boldsymbol{B}}_{\boldsymbol{k}}^{I} \exp(2\sigma t) \Big] \tag{11a}$$

$$\approx \frac{1}{2} \sum_{\boldsymbol{k}} \hat{\boldsymbol{B}}_{\boldsymbol{k}}^{R} \hat{\boldsymbol{B}}_{\boldsymbol{k}}^{R}, \tag{11b}$$

$$KE \approx \frac{1}{2} \sum_{\boldsymbol{k}} \hat{\boldsymbol{u}}_{\boldsymbol{k}}^{I} \hat{\boldsymbol{u}}_{\boldsymbol{k}}^{I}, \tag{11c}$$

where $\star$ denotes a complex conjugate and odd terms have been omitted due to them being zero on average. The imaginary term is neglected in (11a) due to it being much smaller than the other term for the times considered.

Using the approximations for *ME* and *KE*, H_1 is then

$$H_1 = \frac{1}{16\pi^3 \sqrt{ME}\sqrt{KE}} \left| \sum_{\boldsymbol{k}} \hat{\boldsymbol{u}}_{\boldsymbol{k}} \hat{\boldsymbol{B}}_{\boldsymbol{k}}^{\star} \right| \tag{12a}$$

$$= \frac{\exp(\sigma t)}{16\pi^3 \sqrt{ME}\sqrt{KE}} \left| \sum_{\boldsymbol{k}} \Big(\hat{\boldsymbol{u}}_{\boldsymbol{k}}^{R} \hat{\boldsymbol{B}}_{\boldsymbol{k}}^{R} + \hat{\boldsymbol{u}}_{\boldsymbol{k}}^{I} \hat{\boldsymbol{B}}_{\boldsymbol{k}}^{I} \Big) \right|. \tag{12b}$$

As expected, H_1 depends exponentially upon time with the same growth rate as $\hat{\boldsymbol{B}}_{\boldsymbol{k}}^{I}$ and $\hat{\boldsymbol{u}}_{\boldsymbol{k}}^{R}$. The key to this quantity showing the exponential behaviour is that the terms containing both $\hat{\boldsymbol{B}}_{\boldsymbol{k}}^{R}$ and $\hat{\boldsymbol{u}}_{\boldsymbol{k}}^{I}$ within the product $\hat{\boldsymbol{u}}_{\boldsymbol{k}} \hat{\boldsymbol{B}}_{\boldsymbol{k}}^{\star}$ are odd and so are zero when an average is taken. The remaining terms are each formed from one weak, exponentially growing, term and one larger term and it is this that allows H_1 to show that the system is still evolving.

To summarise, I find that cross-helicity grows exponentially for $t \in (1000, 1500)$ due to the forcing term within the cross-helicity evolution equation being stronger than the

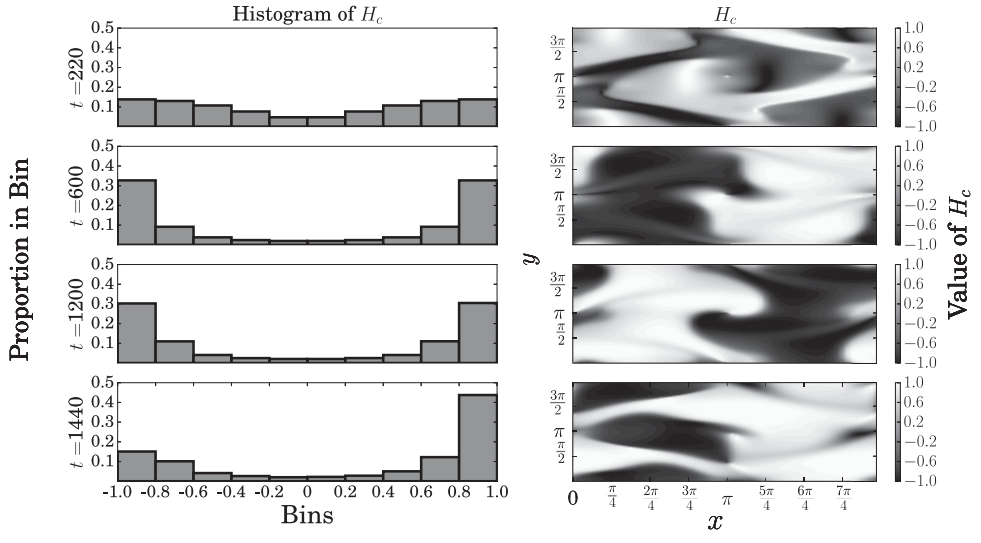

Figure 5. Histograms and $z=0$ contours of H_c for $t = [220, 600, 1200, 1440]$. We see that during the SSS the domain is made up of an almost equal amount of alignment and anti-alignment with the result being a volume average of approximately 0. Towards the end of the SSS the balance between aligned and anti-aligned field becomes skewed towards positively aligned.

combined magnitudes of the diffusion terms. These quantities grow exponentially due to exponential growth of $\hat{\boldsymbol{B}}_{\boldsymbol{k}}^{I}$ and $\hat{\boldsymbol{u}}_{\boldsymbol{k}}^{R}$, the origins of which lies in equations (10b,c).

5. Distribution of alignment within the Archontis dynamo

In this section, I analyse the pointwise distribution of alignment during a Group A run. I define the point-wise normalised cross-helicity H_c to be

$$H_c = \frac{\boldsymbol{u}\cdot\boldsymbol{B}}{|\boldsymbol{u}||\boldsymbol{B}|}. \tag{13}$$

I plot $z=0$ slices of H_c in figures 5 and 6 for various times during a run. I also plot histograms of H_c. Figure 5 shows these quantities at times $t = [220, 600, 1200, 1440]$. These times range from arrival at the SSS ($t=220$) to almost the end of the SSS ($t=1440$). We see that during most of this time period there is a roughly equal balance of positive and negative alignment with the alignment being concentrated near $H_c = \pm 1$. The accompanying contour plots show that the alignment is concentrated into large regions of positive and negative alignment.

We see in the histograms of figure 5 and the first two rows of figure 6 that as we begin to reach the end of the SSS ($t \in (1440, 1500)$) an imbalance forms, with the ratio of aligned to anti-aligned field increasing. In figure 6, I then show $t = [1460, 1480, 1700, 2100]$ covering the onset of the second rapid growth phase until saturation to the final state. We observe that the second growth phase occurs once alignment is almost entirely positive within the domain. Figure 6 further shows that during the second growth phase and the proceeding saturated state the entire domain is made up of positive alignment.

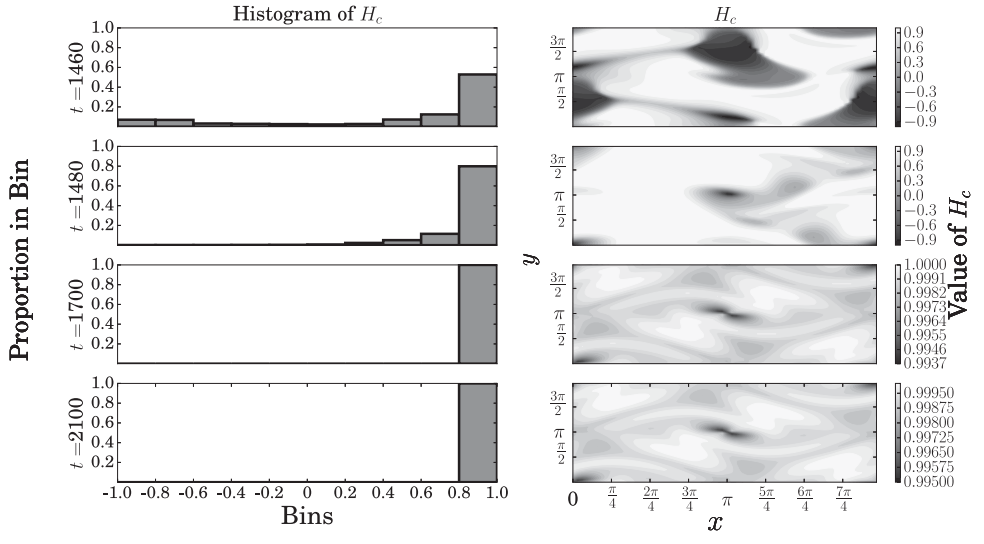

Figure 6. Histograms and $z = 0$ contours of H_c for $t = [1460, 1480, 1700, 2100]$. As we enter the second rapid growth phase the magnetic and flow fields become entirely positively aligned.

The results within figures 5 and 6 therefore show that it is incorrect to view the SSS as having no alignment. The domain is in fact made up of approximately equal amounts of large regions of strong positive and negative alignment. Rather than generating alignment within the domain, the alignment mechanism that induces the second growth phase acts to reverse the alignment of the regions of anti-alignment.

If it is the amount of alignment within the domain rather than the volume average that we are interested in, a sensible alternate measure to (4) is

$$H_2 = \frac{1}{2}\frac{\int_v |\boldsymbol{u}\cdot\boldsymbol{B}|\,\mathrm{d}V}{\sqrt{KE}\sqrt{ME}}, \tag{14}$$

which does not allow for cancellation of positive and negative fields and so gives a measure of the absolute alignment present within the domain. Figure 7 shows this measure of alignment as well as the old measure and the kinetic and magnetic energies. We see that upon entering the SSS, H_2 saturates to a value of approximately 0.8 where it stays until it increases again when the alignment increases immediately prior to the second growth phase. Therefore, by this new measure the change in alignment prior to the second growth phase is more modest.

To summarise, it is found that the lack of volume averaged alignment seen within a Group A run prior to the second growth phase is caused by a balance between regions of strong positive and negative alignment. When we take this into consideration by defining a new alignment measure, H_2, the increase in alignment is much more modest.

6. Addition of time dependence to the Archontis dynamo

The aim of this section is to investigate whether an aligned and equipartition state is produced as different variables are introduced to the Archontis forcing. The number of known

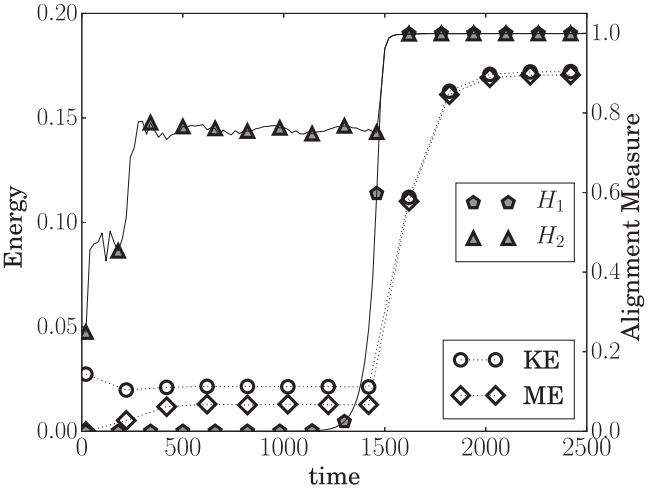

Figure 7. *KE* and *ME* using the left axis with H_1 and H_2 using the right axis. We see that H_2 reaches a value of 0.8 immediately prior to saturation of the energies to the first SSS and that this remains approximately steady until the second rapid growth phase. As we have previously seen, alignment is weak during the first SSS. From figure 5, we see that this is in fact due to the amount of positive and negative alignment within the domain being approximately equal. Immediately prior to the second rapid growth phase, the absolute alignment and the alignment become equal. This occurs due to an increase in the proportion of alignment within the domain that is positive over the proportion that is negative, see figure 6.

forcings which produce aligned states is small and no method currently exists for predicting whether a forcing will produce an aligned state. As such, it is unknown whether the steady, highly symmetric nature of the Archontis forcing is essential to producing such states. Altering the Archontis forcing in a controlled manner is therefore the simplest method of identifying whether or not these features are required to produce aligned states in nonlinear dynamos.

To introduce asymmetry and time dependence, I alter $\boldsymbol{F}_A$ in two ways. I use a parameter to make each new forcing increasingly different to $\boldsymbol{F}_A$, and examine the resulting energies and alignment. These new forcings are denoted $\boldsymbol{F}_R$ and $\boldsymbol{F}_\xi$. Here, I will primarily focus on how the alignment and energies change. For information on the three-dimensional structure of the magnetic field in these dynamos, see Miller (2019).

Diffusivities η and ν were chosen to be 1/100 so as to be able to compare results to those within section 3 as well as those obtained by Cameron and Galloway (2006a). Doubling η and halving $P_m = \nu/\eta$ for $\boldsymbol{F}_R$ produced results similar to those for $\nu = \eta = 1/100$. Average energy for each parameter value is calculated by taking a time average once a statistically steady state is reached.

The first adaptation to the Archontis forcing

$$\boldsymbol{F}_R = \nu \left[\sin z,\ \sin(x + R\cos t),\ \sin(y + R\sin t)\right] \tag{15}$$

differs by the addition of a circular polarisation. This method of adding time dependence to a steady field has been used previously within kinematic dynamo simulations by Galloway and Proctor (1992). It has also been used to add time dependence to ABC forcings by

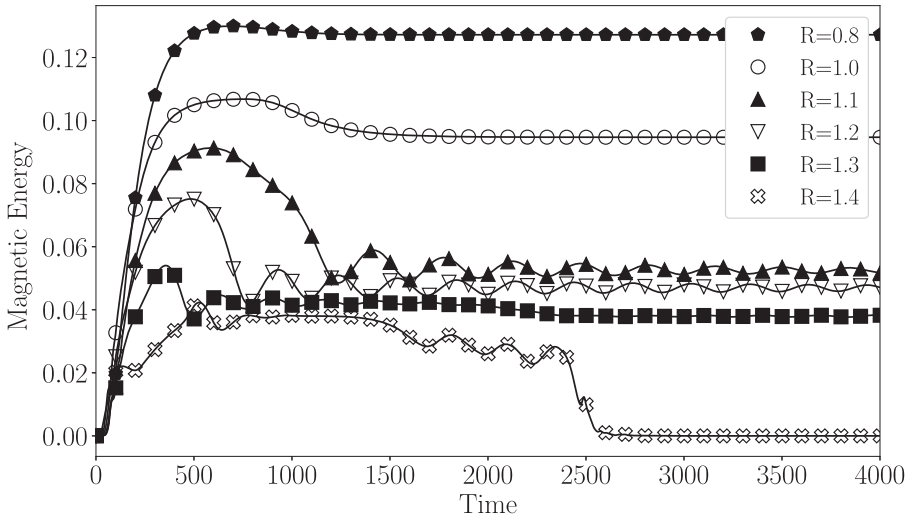

Figure 8. Plot of *ME* versus time for $\boldsymbol{F}_R$. For $R \leq 1$, the energy reaches an almost completely steady state. Small oscillations with period 2π are present due to the periodicity of the forcing. However, they are negligible in amplitude. For $1.0 < R < 1.4$, the circular polarisation in the forcing disrupts the energy evolution more significantly. However, a statistically steady state is eventually reached with the time dependence decreasing at large time.

Brummell *et al.* (2001), although the dynamos produced were very different to the ones we observe here.

Simulations were performed using $\boldsymbol{u}_0 = \boldsymbol{F}_R/\nu$ and a random seed field for the magnetic field. R was increased from zero in increments of 0.1 until a value, $R = R_c$, no longer allowed for significant *ME* at large time. The influence of initial conditions was checked by comparing the results against simulations began with $\boldsymbol{u}_0 = \boldsymbol{B}_0 = \boldsymbol{F}_R/\nu$ and simulations where a seed magnetic field is introduced only after the flow has evolved to a steady state. No difference was found in R_c. For each $R < R_c$ the field structure and energies (at large time) also did not vary between the initial conditions.

In figure 8, I show time series of the ME for a number of values of R. For all parameter values, both energies keep a 2π periodicity (with small amplitude) due to the time dependence of the forcing. For $0 < R \leq 1$, the energies quickly asymptote to an almost steady state. Above $R = 1$, the energies have more time dependence but eventually become statistically steady. This continues until the critical parameter value ($R = 1.4$) where the *ME* decays to zero at large time. Figure 8 therefore shows that even after the addition of significant time dependence, a surprisingly steady state is achieved by this dynamo.

The $z = 0$ contours of $|\boldsymbol{B}| = \sqrt{\boldsymbol{B}_x^2 + \boldsymbol{B}_y^2 + \boldsymbol{B}_z^2}$ in figure 9 show that until $R = 1$ the magnetic field contours resemble those of $\boldsymbol{F}_A$, $\boldsymbol{u}$ and $\boldsymbol{B}$ in the Archontis dynamo. In particular, the strong field is clustered in the same regions. As such, the magnetic field is evolving to a similar state to that which it evolves to in the Archontis dynamo. The contours of the flow (not shown) are almost identical to those of the magnetic field. Beyond $R = 1$, the structure of the magnetic field becomes significantly different to that of $\boldsymbol{F}_A$ with the regions of strongest field become significantly distorted.

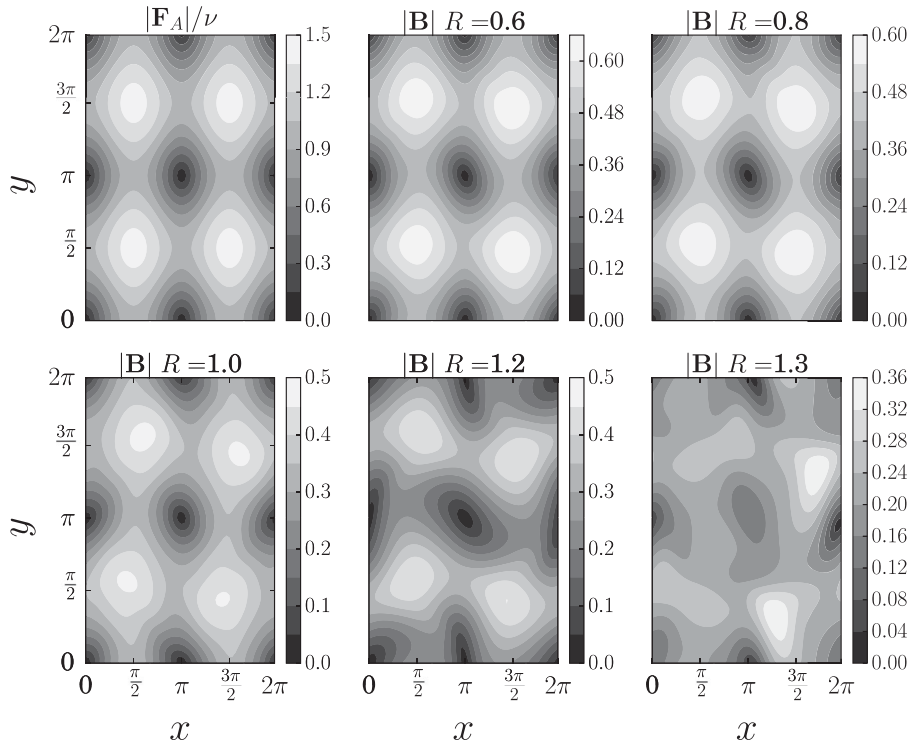

Figure 9. Plot showing $z = 0$ contours of $|\boldsymbol{F}_A|$ and $|\boldsymbol{B}|$ at various R for simulations with the forcing $\boldsymbol{F}_R$. For $R < 1$, the field structure closely resembles that of $\boldsymbol{F}_A$ as well as that of $\boldsymbol{u}$ and $\boldsymbol{B}$ during the Archontis dynamo. However, as $R \to R_c$ the regions of strongest field become distorted and this structure breaks down, although alignment is still strong even at $R = 1.3$.

In figure 10, I show the average energy and alignment in the final state for $0 < R \leq R_c$. We see that the average energy decreases as $R \to R_c$ and that the flow and magnetic field remain almost perfectly aligned and at equipartition up until R_c. These simulations show that an aligned and equipartition state can be reached even after the introduction of significant time dependence to the forcing. The addition of circular polarisation to the Archontis dynamo results in a decrease in average energy and eventually distortion of the magnetic field structure. Until the dynamo fails at R_c, the states produced by the dynamo have the flow and magnetic field almost perfectly aligned. The simultaneous failure of the alignment and the dynamo show that, for this particular family of forcings, one cannot exist without the other.

As the majority of the magnetic field structures produced by $\boldsymbol{F}_R$ are similar to those produced by $\boldsymbol{F}_A$, a sensible extension is to see if aligned states can be produced with different magnetic field structures. The second forcing, $\boldsymbol{F}_\xi$, that I examine therefore alters the x dependent component of $\boldsymbol{F}_A$. The idea is to see if aligned states can be produced with this asymmetry at all, and if so whether they resemble $\boldsymbol{F}_A$, or the new forcing

$$\boldsymbol{F}_\xi = \nu \left[\sin z,\ (1+\xi)\sin x,\ \sin y\right], \tag{16}$$

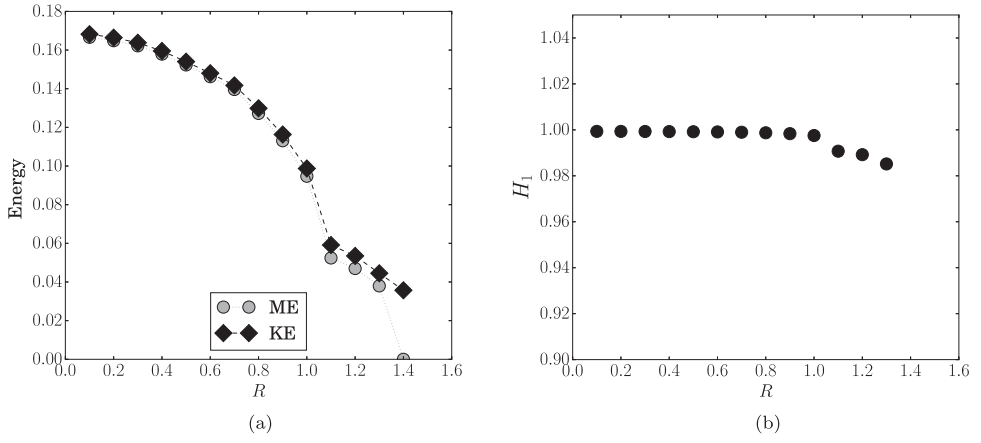

Figure 10. Energy and H_1 as R is varied for simulations using the forcing $\boldsymbol{F}_R$. (a) Kinetic and magnetic energy. We see that both energies decrease with increasing radius. (b) Alignment is seen to decrease slightly beyond $R = 1$ but they remain highly aligned.

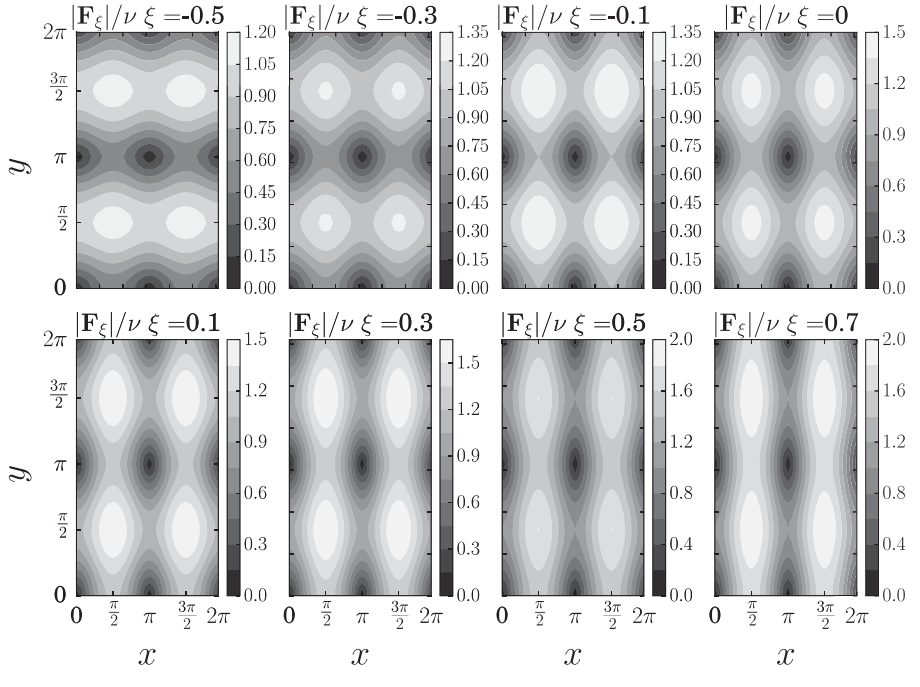

Figure 11. $z = 0$ contours of $\boldsymbol{F}_\xi$. For $\xi < 0$, the field is elongated in the x direction, whereas when $\xi > 0$ the field is elongated in the y direction.

for which the $z = 0$ contours are shown in figure 11. Simulations with this forcing were performed using the initial condition $\boldsymbol{u}_0 = \boldsymbol{F}_\xi/\nu$ and $\boldsymbol{B}_0 = \boldsymbol{F}_\xi/\nu$ as this speeds up arrival to the final state. I note, however, that both fields still undergo significant evolution before arriving at their final state and that for $\xi > 0.3$ the energies oscillate with a significant amplitude in the final state.

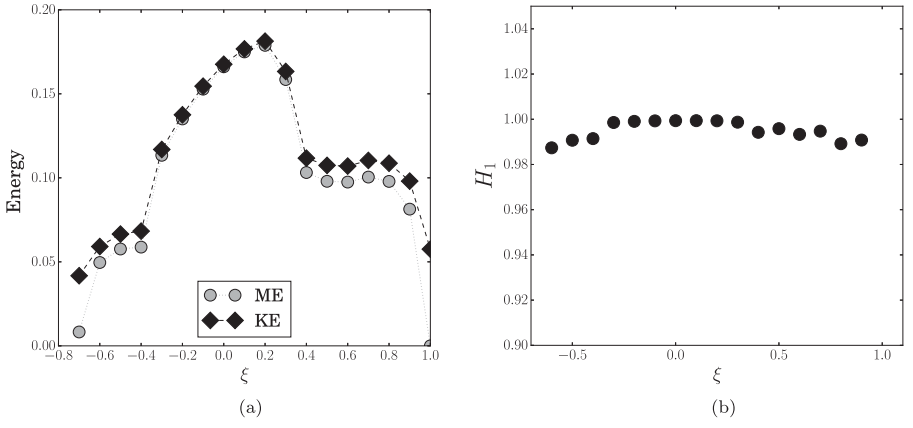

Figure 12. Energy and H_1 as ξ is varied for simulations using the forcing $\boldsymbol{F}_\xi$. (a) The energies decrease far from $\xi = 0$ but remain approximately at equipartition until the dynamo fails. (b) Alignment is close to maximal for all values which yield dynamo action.

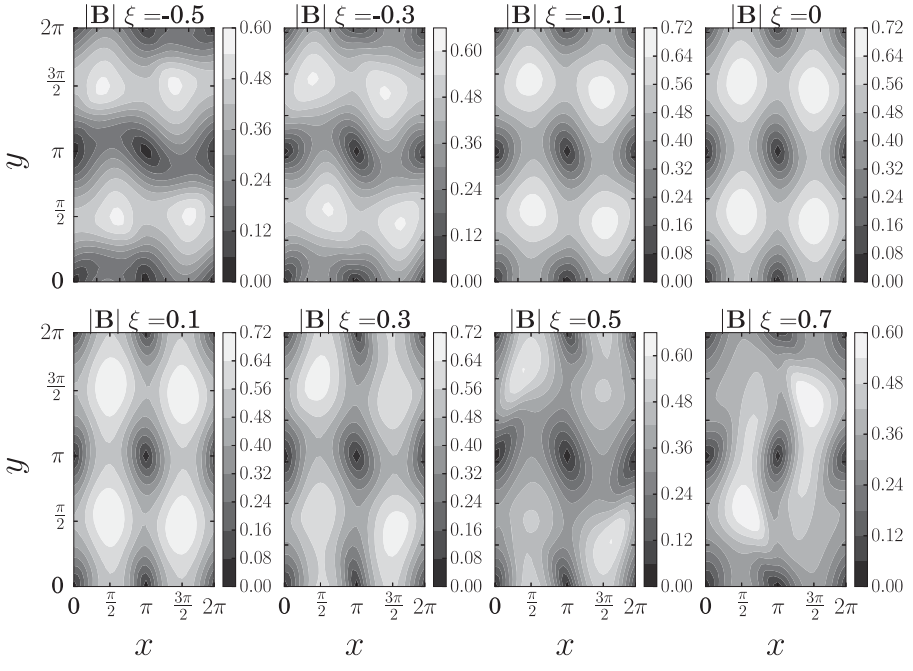

Figure 13. $z = 0$ contours of $|\boldsymbol{B}|$ for a variety of ξ. For $|\xi|$ close to zero the contours resemble those of the forcing, with elongation in x for negative ξ and elongation in y for positive ξ.

The time averaged energies in the final state and H_1 are shown in figure 12. As the parameter gets further from zero, the value of the average energy eventually decreases (there is a small increase for $\xi \in [0, 0.2]$). As with $\boldsymbol{F}_R$, strong alignment and approximate equipartition are seen for all values of the parameter where *ME* remains significant at large time.

In figure 13, I show $z = 0$ contours of $|\boldsymbol{B}|$ at large time. Comparing these contours to the contours of the forcing in figure 11 we see that for $|\xi|$ close to zero the contours have the

same general features as those of the forcing. However, for large positive values of ξ the resemblance of the field to the forcing becomes much weaker.

Examining dynamos forced by $\boldsymbol{F}_\xi$ has therefore shown that asymmetric aligned states (close to those produced by the Archontis dynamo) can be found by introducing small amounts of asymmetry to the forcing. This shows that the strong symmetry of the Archontis forcing is not necessary to produce an aligned state.

In summary, simulations with two modifications to the Archontis forcing have shown that aligned dynamos with equipartition energy are produced even after significant time dependence and asymmetry are introduced to the forcing. Whilst this is only a first step in identifying more complex forcings which produce aligned dynamos, it is suggestive that they do indeed exist.

7. Discussion

The Archontis dynamo is important as it is the first example of a nonlinear dynamo which achieves saturation to a final equipartion state via a mechanism which appears to be preceded by almost perfect alignment between the flow and magnetic fields. As such, the dynamo is able to generate magnetic energy at the same order of magnitude as the kinetic energy. During previous work examining the dynamo, a number of questions were raised, two of which I have addressed here. The first concerns whether or not any physical meaning could be attached to the statistically steady state seen within Cameron and Galloway (2006a). In section 3, I have shown that this SSS is a result of a choice of initial conditions, the significance of this being that we may conclude that the presence of this state is not necessary to achieve the final steady state.

Furthermore, in examining the pointwise distribution of the alignment, I showed that the lack of global alignment before the final state is a result of cancellation of large amounts of alignment rather than a broader spectrum of alignment magnitudes within the domain. By defining a new measure of alignment, I was able to show that the increase is much more modest.

In adding time dependence and asymmetry to the Archontis forcing, I have also shown that forcings involving these factors can also produce aligned dynamos. In all of the dynamos examined, dynamo action was only found when alignment was strong. As such, alignment clearly plays a crucial role in achieving significant magnetic energy at large time for this family of dynamos. The exact reason for this is, however, still unknown.

Whether or not a high number of aligned equipartition dynamos exist is still an open question. Although Cameron and Galloway (2006b) show two further examples, there is at present no way of predicting which forcings will yield aligned states and this makes them difficult to study. However, the role of alignment in these dynamos (along with the equipartition of energy) makes them unique amongst nonlinear dynamos and intriguing enough to warrant further research.

Acknowledgments

I would like to thank J. Mason and A.D. Gilbert for many useful comments and discussions. The research data supporting this publication are openly available from the [University of Exeter's institutional repository] at: [https://doi.org/10.24378/exe.1603]

Disclosure statement

No potential conflict of interest was reported by the author.

Funding

The work was supported by an EPSRC studentship entitled "Magnetohydrodynamic Turbulence and Dynamos" Award Reference: 1636452.

References

Archontis, V., Linear, non-linear and turbulent dynamos. Ph.D. Thesis, University of Copenhagen, Denmark, 2000.

Archontis, V., Dorch, S.B.F. and Nordlund, A., Nonlinear MHD dynamo operating at equipartition. *Astron. Astrophys.* 2007, **472**, 715–726.

Brummell, N.H, Cattaneo, F. and Tobias, S.M., Linear and nonlinear dynamo properties of time-dependent ABC flows. *Fluid Dyn. Res.* 2001, **28**, 237–265.

Cameron, R. and Galloway, D., Saturation properties of the Archontis dynamo. *Mon. Not. R. Astron. Soc.* 2006a, **365**, 735–746.

Cameron, R. and Galloway, D., High field strength modified ABC and rotor dynamos. *Mon. Not. R. Astron. Soc.* 2006b, **367**, 1163–1169.

Dorch, S.B.F. and Archontis, V., On the saturation of astrophysical dynamos: Numerical experiments with the no-cosines flow. *Sol. Phys.* 2004, **224**, 171–178.

Galanti, B., Sulem, P.L. and Pouquet, A., Linear and non-linear dynamos associated with ABC flows. *Geophys. Astrophys. Fluid Dyn.* 1992, **66**, 183–208.

Galloway, D.J. and Proctor, M.R.E., Numerical calculations of fast dynamos in smooth velocity fields with realistic diffusion. *Nature* 1992, **356**, 691–693.

Galloway, D.J., Fast dynamos. In *Advances in Nonlinear Dynamos*, edited by A. Ferriz-Mas and M. Nunez, pp. 37–59, 2003 (Taylor & Francis: New York, NY).

Galloway, D.J., Nonlinear Dynamos. In *Astrophysical Dynamics: From Stars to Galaxies Proceedings IAU Symposium No. 271*, edited by N.H. Brummell, A.S. Brun, M.S. Miesch and Y. Ponty, pp. 297–304, 2010 (Cambridge University Press: Cambridge, UK).

Galloway, D., ABC flows then and now. *Geophys. Astrophys. Fluid Dyn.* 2012, **106**, 450–467.

Gilbert, A.D., Ponty, P. and Zheligovsky, V., Dissipative structures in a nonlinear dynamo. *Geophys. Astrophys. Fluid Dyn.* 2011, **105**, 629–653.

Krstulovic, G., Thorner, G., Vest, J.-P, Fauve, S. and Brachet, M., Axial dipolar dynamo action in the Taylor-Green vortex. *Phys. Rev. E* 2011, **84**, 066318.

Larmor, J., How could a rotating body such as the Sun become a magnet? *Rep. Br. Assoc.* 1919, **87**, 159–160.

Miller, D., Alignment and Structure in MHD Dynamos, Ph.D. Thesis, University of Exeter, United Kingdom, 2019.

Tanner, S.E.M. and Hughes, D.W., Fast-dynamo action for a family of parametrized flows. *Astrophys. J.* 2003, **586**, 685–691.